Aftershock Sequence of the 2018 M_w 6.4 Hualien Earthquake in Eastern Taiwan from a Dense Seismic Array Data Set

by Hao Kuo-Chen, Zhuo-Kang Guan, Wei-Fang Sun, Pei-Yu Jhong, and Dennis Brown

ABSTRACT

The February 2018 M_w 6.4 earthquake in eastern Taiwan caused extensive damage in Hualien City. Although damaging earthquakes are common in this region, there are relatively few permanent seismic stations deployed. Two days after the mainshock, we deployed 70 temporary seismic stations around Hualien City for 12 days (8–19 February), and station spacing was 1–5 km. During this time, 2192 aftershocks were located from which 580 focal mechanisms were determined. The aftershock sequence extended about 25 km southwestward from the epicenter of the mainshock into the Longitudinal Valley and to depths between 5 and 15 km. Earthquake hypocenters indicate that the aftershocks took place along a near-vertical to steeply west-dipping plane in the north that becomes more diffuse in the south. Focal mechanisms are predominantly extensional, different than the left-lateral strike slip with thrust-component faulting of the mainshock. Very few events occurred in the uppermost crust at depths of less than 5 km, and their focal mechanisms are left-lateral strike-slip faulting. From the mainshock to the aftershocks, the stress changed rapidly from a north-northwest-oriented compressional axis (P axis) to the same direction for the extensional axis (T axis).

Electronic Supplement: Tables of aftershocks and focal mechanisms obtained in this study and figures of M_w determination via manual spectral analysis and result of automatic spectral analysis.

INTRODUCTION

On 6 February 2018, an M_w 6.4 earthquake occurred at 10 km depth in the northeastern offshore region of Hualien City that caused the collapse of 4 buildings and ~300 casualties. Because this region is located along the intersection of two plates in the active plate boundaries, large and damaging earthquakes are common. For instance, there were three magnitude 7 events and two magnitude 6 events between 1951 and 1986 near Hualien City, and several magnitude 7 events occurred offshore east of Hualien since 1920 (Fig. 1a; Theunissen *et al.*, 2010) that caused significant damage. From the U.S. Geological Survey moment tensor catalog (see Data and Resources), the mainshock is a left-lateral strike-slip fault with a high-dipping angle to the west (strike, 209°; dip, 72°; rake, 22°; Fig. 1a). According to the large (M_L 3–5) aftershocks recorded by the fast earthquake reporting system of Central Weather Bureau (see Data and Resources), from 6 to 20 February, the aftershock sequence propagated southward from the mainshock and shallowed from depths of greater than 10 km to less than 5 km (Fig. 1b). Most of the areas damaged during the mainshock are located near the east-dipping Milun and Lingding faults (Fig. 1b). These faults have opposing dips to that calculated from the mainshock focal mechanism, raising an intriguing question as to how the active fault systems at the surface are linked to those images by the aftershock sequence at depth. In this study, we present the analyses of 2192 aftershocks and 580 focal mechanisms, with the aim of investigating how the surface deformation and the deep structure are linked.

TECTONIC SETTING

The Taiwan orogeny is forming along a complex plate boundary in which the Eurasian plate (EUP in Fig. 1a) is subducting eastward beneath the Philippine Sea plate (PSP in Fig. 1a) in southern Taiwan at a latitude of ~22.8° N, whereas the PSP is subducting northwestward beneath the EUP along the Ryukyu trench (RkT in Fig. 1a) in northeastern offshore Taiwan. These two subducting plates can be observed by Wadati–Benioff zones (Tsai, 1986). The Longitudinal Valley (LV) serves as a suture zone between two plates on land. In the west side of the LV, the Central Range (CeR) is a metamorphic terrane of the EUP, whereas in the east side of the LV, the Coastal Range (CoR) is mainly composed of volcanic rocks of the PSP (Fig. 1b). The intensive collision between the two plates occurs along the LV. Because of the oblique collision, the LV

doi: 10.1785/0220180233

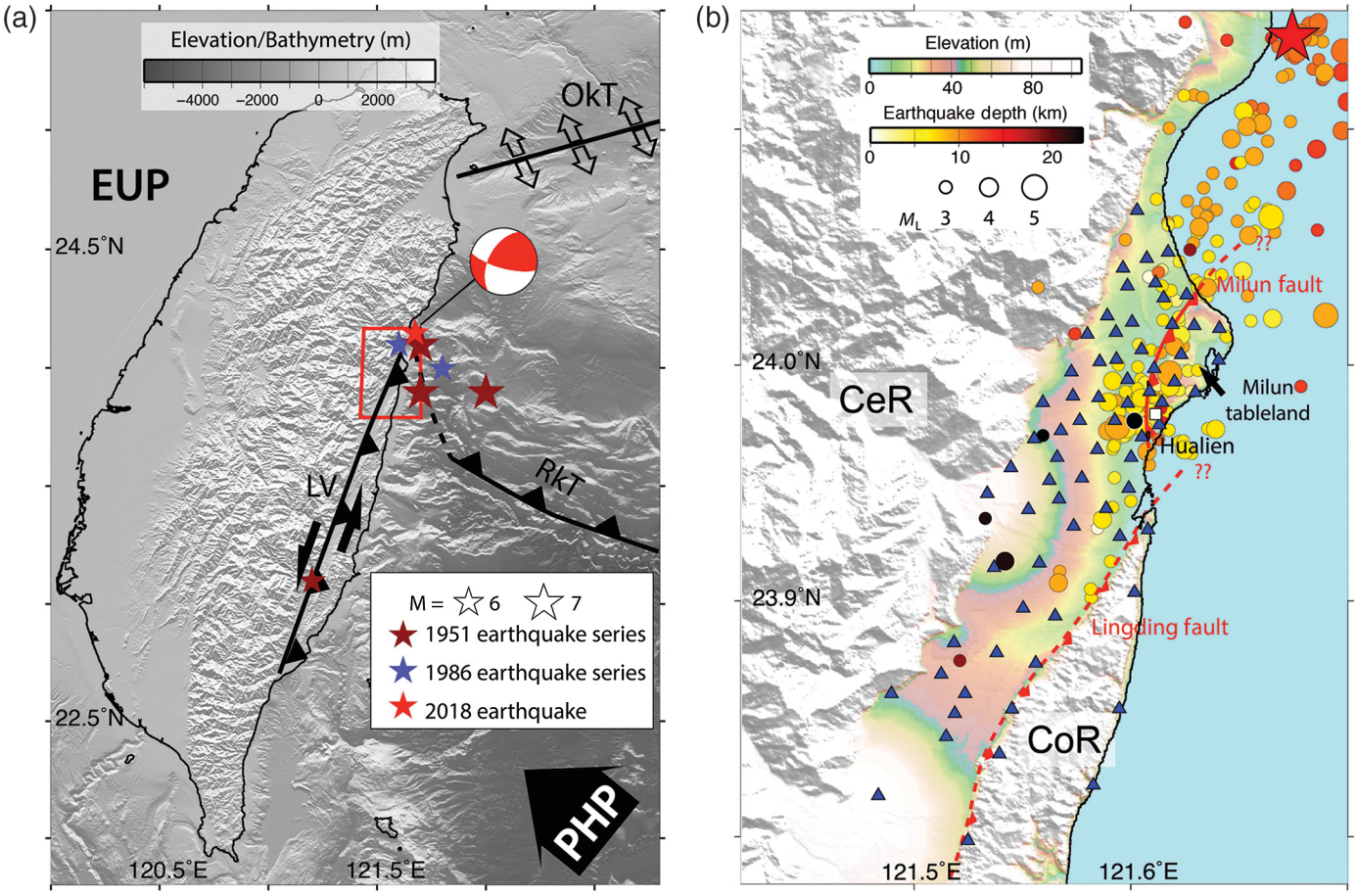

▲ **Figure 1.** (a) Tectonic setting of Taiwan and historical large earthquakes in the Hualien area. The focal mechanism of the 2018 Hualien earthquake from the U.S. Geological Survey. RkT, Ryukyu trench; LV, Longitudinal Valley; OkT, Okinawa trough; EUP, Eurasian plate; PHP, Philippine Sea plate; CeR, Central Range; CoR, Coastal Range. (b) The red star and circles are the mainshock and large ($M_L > 3$) aftershocks, respectively, based on the fast earthquake report of the Central Weather Bureau from 6 to 20 February. The red solid and dashed lines are the Milun active fault and inferred Lingding active fault, respectively. White square, permanent seismic station; blue triangle, temporary seismic stations.

and RkT are mainly reverse-fault systems with a sinistral component and a small dextral component, respectively. The Hualien region, north of the LV, situated at the transition from collision to subduction, results in complex seismogenic structures, whereas the region south of the LV has a relatively simple structure (Kuochen *et al.*, 2004; Wu *et al.*, 2009; Chin *et al.*, 2016; Shyu *et al.*, 2016). Although the average principal compressional axis inferred from focal mechanisms is northwest trending and associated with the PSP motion (Wu *et al.*, 2009), it is hard to define the earthquake clusters as main seismogenic structures (Kuochen *et al.*, 2004; Shyu *et al.*, 2016).

Based on relocated earthquakes from 1991 to 2002, Kuochen *et al.* (2004) showed that two types of earthquake clusters can be identified with respect to the focal mechanisms due to the PSP initially subducting northwestward in the Hualien region: one is a normal-faulting type at shallow depths (within 10 km) related to the PSP bending, and the other one is a west-dipping thrust type ranging from shallow to deep depths (0–40 km) and is related to the subduction of the PSP. Recently, Shyu *et al.* (2016) used the relocated earthquakes from 1991 to 2010 to further investigate the Hualien region using a 3D velocity model (Wu *et al.*, 2007). In addition to the earthquake clusters reported by Kuochen *et al.* (2004), the authors determined new earthquake clusters with mostly reverse faulting at shallow depths (above 15 km), based on aftershock sequences of two moderate events ($M_L \sim 4$) in 2009 and 2010. Among the previous studies addressed above, the seismogenic structures in the Hualien region are mainly controlled by northwest–southeast compressional stress, with several earthquake clusters reflecting the current plate configuration of the PSP and EUP.

The LV fault system at the surface suggests that several branch faults are associated with the system; the major ones are the Milun and Lingding faults (Fig. 1b; Hsu, 1962). The Milun fault is considered to be a left-lateral reverse fault with a high dip angle toward the east (Hsu, 1955; Yu *et al.*, 1990). In 1951, the M_L 7.3 Hualien earthquake ruptured this fault at ~1.2 and 2 m in vertical and left-lateral displacements, respectively (Hsu, 1955). The Lingding fault is located along the

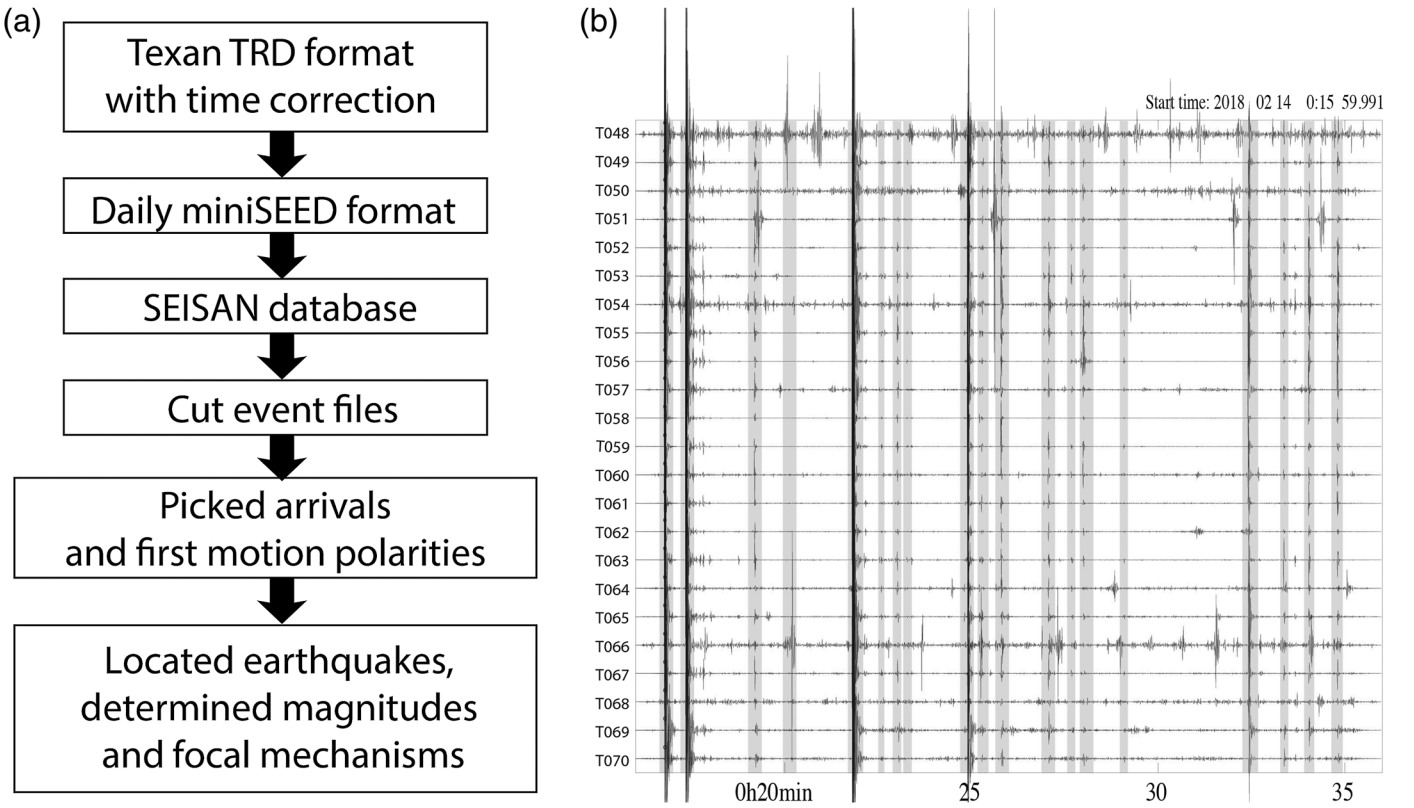

▲ **Figure 2.** (a) Data processing flow from raw data to SEISAN software. (b) Example of seismic waveforms recorded in a 20-min window in the temporary seismic network.

western edge of the CoR, but fault traces are not found in the field, which could be covered by alluvium fans (Lin *et al.*, 2009). Based on previous studies, this fault, which is part of the LV fault system, is also a left-lateral reverse fault (Lin *et al.*, 2009; Shyu *et al.*, 2016).

DATA AND ANALYSIS

Two days after the mainshock, we started to deploy 70 vertical-component short-period seismic stations (4.5 Hz geophone with a Texan recorder) around Hualien, with a spacing of 1–5 km on 8 February and finished the deployment on the next day (Fig. 1b; for a complete list of station locations, see Ⓔ Table S1, available in the electronic supplement to this article). We set up Texan recorders to record continuous waveforms with a 100 Hz sampling rate for 12 days until 19 February, considering the battery capacity. The data processing procedure is shown in Figure 2a. We converted the Texan data format (TRD) via a time correction to the daily miniSEED format. We then used SeisAn Earthquake analysis software (SEISAN) to establish the database and process the data (Havskov and Ottemoller, 1999). Because most of the aftershocks occurred around this temporary seismic network, we were able to record high-quality seismic waveforms (Fig. 2b) to locate earthquakes and determine magnitudes and focal mechanisms (Fig. 3) of events. Figure 2b shows an example of 20 events that occurred within 20 min on 14 February. We used the HYPOCENTER program (e.g., Lienert *et al.*, 1986) and a Taiwan 1D velocity model from Chen and Shin (1995) to locate earthquakes. After removing the instrumental response, we determined the moment magnitude (M_w) using spectral analysis with a 1D attenuation model from Chen *et al.* (1996) and Chen (1998). See the Ⓔ electronic supplement for a short description of the procedure for calculating spectral M_w. The detailed procedure is described in Havskov and Ottemoller (2010). In total, 4222 events were clearly detected, and 2192 events were manually picked during the deployment; some arrivals of unpicked events were buried in coda waves of previous earthquakes. The data set contains 58,480 *P*-wave and 2704 *S*-wave arrivals. There are significantly fewer *S*-wave arrivals than *P*-wave arrivals because only the vertical component of the seismometer was used. However, we tried to pick at least one clear onset *S*-wave arrival for each event to better constrain the depths of the earthquakes (for a complete list of aftershocks, see Ⓔ Table S4).

In terms of instruments, a geophone was used to set a negative value for ground motion moving upward, as industrial standard, which is opposite to the design of seismometers (e.g., Brown *et al.*, 2000). Because we used the first *P*-wave polarity to determine focal mechanisms of small-to-moderate magnitude earthquakes, we further validate the polarities of geophones by plotting the first *P*-wave motions determined in this study with the focal mechanism from real-time moment tensor (RMT) inversion (Lee *et al.*, 2014). As shown in Figure 3a, the distribution of the compressions (C) and dilatations (D) from first *P*-wave

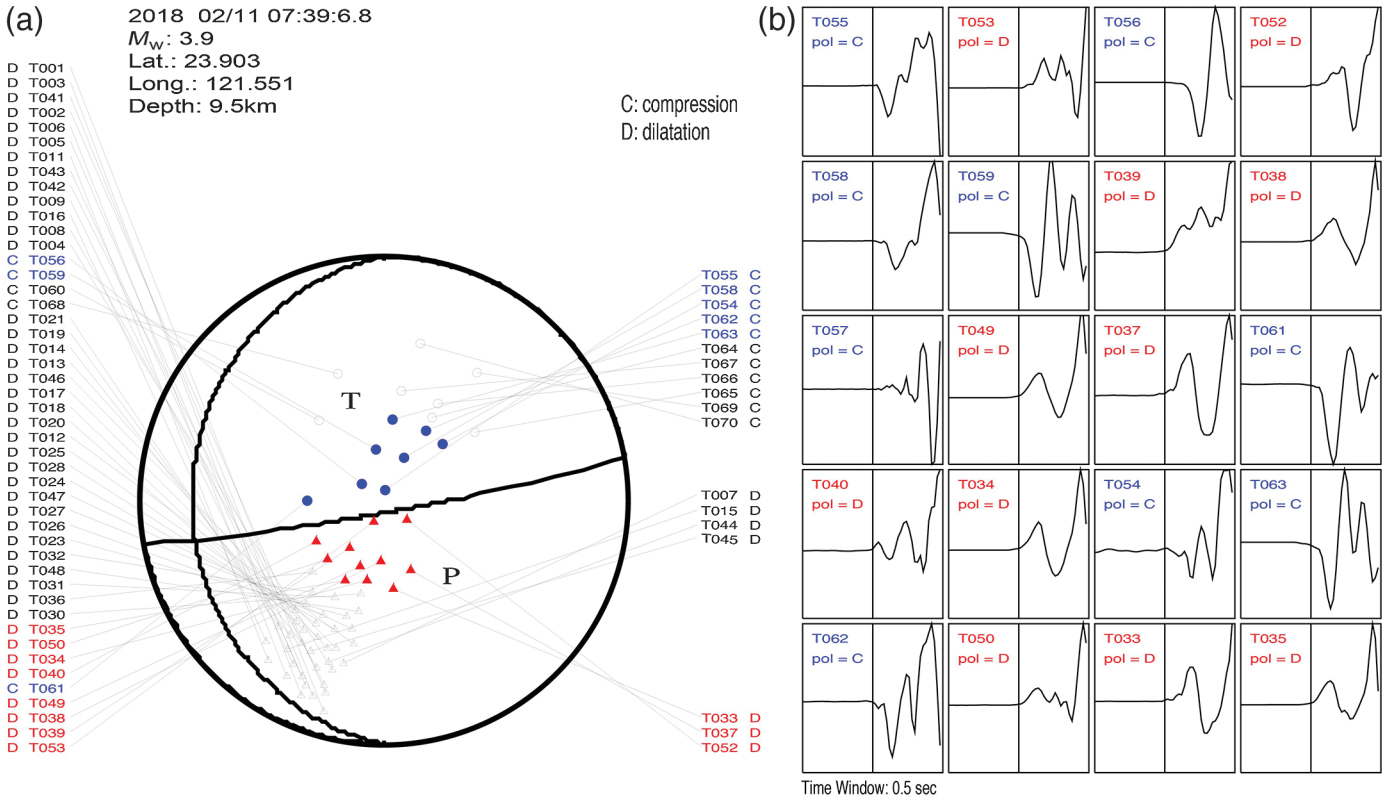

▲ **Figure 3.** (a) Comparison of a focal mechanism from the real-time moment tensor inversion system (see Data and Resources) and fir 13 *P*-wave polarities from this study. Circle, compression (C) of the first *P*-wave polarities; triangle, dilatation (D) of the *P*-wave polarities; station labeled with blue text and circle, compression of the first *P*-wave polarity waveform shown in (b); station labeled with red text and triangle, dilatation of the first *P*-wave polarity waveform shown in (b). (b) Reverse polarities of seismic waveforms recorded by geophones as industrial standard, that is, negative values for compression and positive values for dilatation.

motions coincides with that from the RMT of the M_w 3.9 earthquake on 11 February. The first *P*-wave polarities can be clearly identified but show reverse polarities, that is, negative values for compression and positive values for dilatation (Fig. 3b). We then used the FPFIT program (Reasenberg and Oppenheimer, 1985) to determine first *P*-wave-motion focal mechanisms. In total, 580 focal mechanisms were determined in this study (for a complete list of focal mechanisms, see Ⓔ Table S5).

RESULTS

A total of 1444 events with at least nine arrivals are located within the temporary seismic network (GAP ≤ 180°) and 748 events are outside of the network (Fig. 4a). Statistically, the magnitudes (M_w) of aftershocks within the seismic network determined in this study mostly range from 1.0 to 2.5, and the standard errors of the means in vertical location (ERZ), 6 in horizontal location (ERH), and *root-mean-square* error in arrival time of the aftershock locations are 2.19 ± 1.81 km, 1.79 ± 1.08 km, and 0.08 ± 0.03 s, respectively. However, the results in the study may further improve using a 3D velocity model, considering the complex tectonics of the Hualien area. In terms of the small location uncertainties obtained, we expect that the overall pattern of the results will remain similar. In this study, we focused on the events distributed within the network that have a better quality with respect to the earthquake location and contain most event clusters. The north-northwest-striking aftershocks, similar to the large aftershocks reported by the Central Weather Bureau (Fig. 1b), are distributed from the northern part of the Milun fault to the northern part of the Lingding fault, and the depths mostly are > 15 km. The three northwest–southeast cross sections roughly perpendicular to the strike of the aftershocks show the spatial variation of the aftershocks from north to south (Fig. 4f–h). Two northern cross sections (Fig. 4f,g) show that the event cluster is nearly vertical, dipping to the west. In the southern cross section (Fig. 4h), the event 7 cluster is more scattered than that of the other two cross sections. It is interesting to note that shallower events (< 5 km) only occurred in the middle cross section (Fig. 4g). Based on the comparison of the background seismicity (gray crosshairs) from 1990 to 2015 (Shyu *et al.*, 2016), the west dipping of the aftershocks (red circles) differs from that of the background seismicity (Fig. 4f–h) beneath the Hualien area.

In total, 523 focal mechanisms with GAP ≤ 180° and 57 with GAP > 180° were determined in this study. The

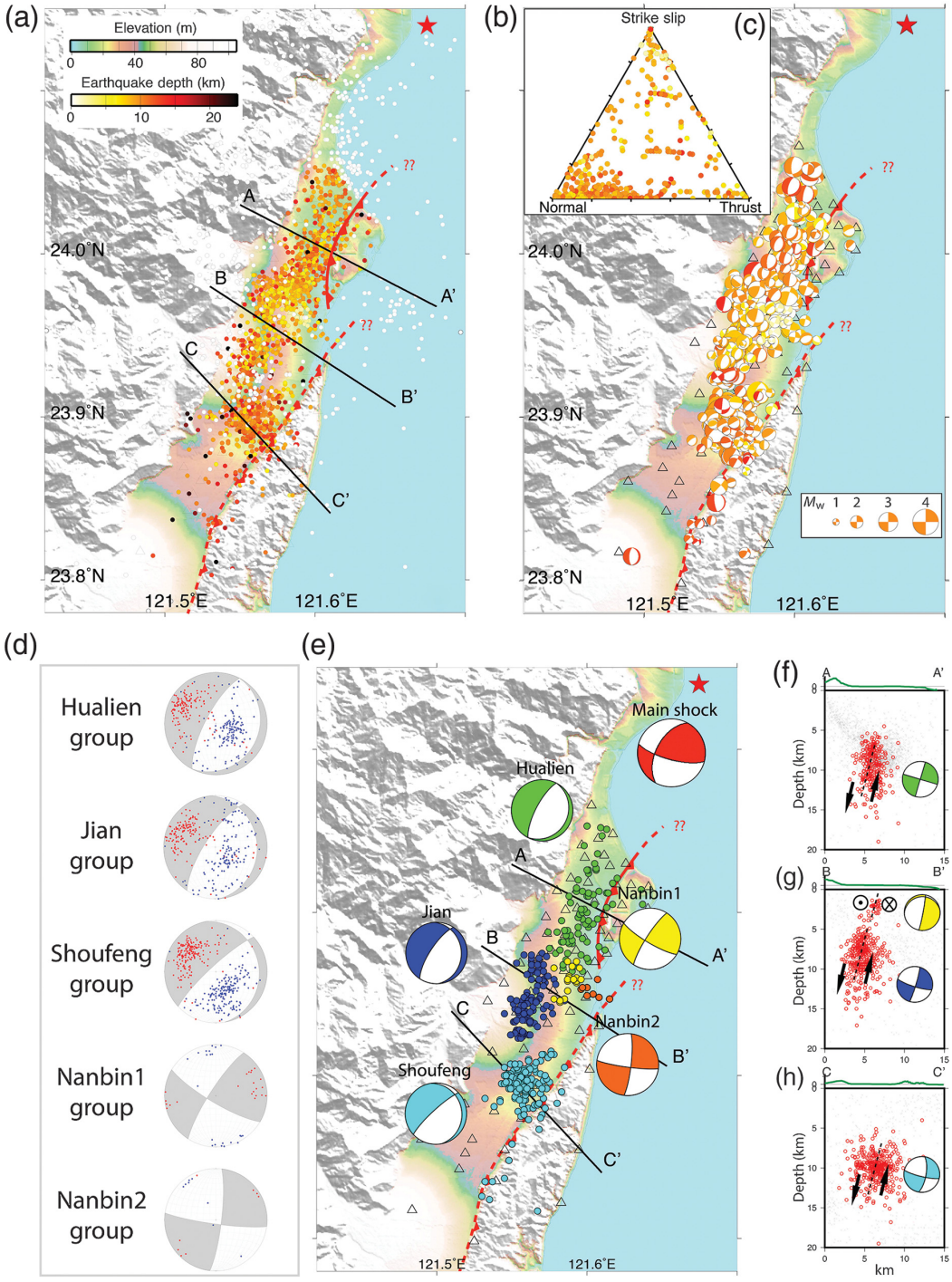

▲ **Figure 4.** (a) Aftershock sequence recorded in the temporary seismic network from 8 to 19 February. Color-coded circle, earthquakes located with GAP ≤ 180°; white color-coded circle, earthquakes located with GAP > 180°. Solid lines show the map view of three cross sections in (f–h). (b) Focal mechanisms based on the first *P*-wave polarities. (c) Focal mechanisms plotted in a Frohlich triangle diagra14 (Frohlich, 1992). (d) Composite focal mechanisms (CFMs) obtained from the averaged P (blue circles) and T axes (red circles). (e) CFMs of five groups and the focal mechanism of the mainshock. The different color-coded circles show the different focal-mechanism groups, and the CFM from its own group is plotted with the same color as the circles. (f) A–A′ cross section with background seismicity (gray crosshairs), aftershocks (red circles), and CFM of the Hualien group. Black dashed line, inferred fault plane based on aftershocks and the CFM. (g) B–B′ cross section with background seismicity (gray crosshairs), aftershocks (red circles), and CFMs of the Jian (blue) and Nanbin1 (yellow) groups. Black dashed lines, inferred fault planes based on aftershocks and the CFMs. (h) C–C′ cross section with background seismicity (gray crosshairs), aftershocks (red circles), and CFM of the Shoufeng (cyan) group. Black dashed line, inferred fault plane based on aftershocks and the CFM.

magnitudes (M_w) range from 1.0 to 4.1. To have better focal mechanism qualities consistent with the previous paragraph, we only describe the focal mechanisms within the seismic network (Fig. 4b). The average errors of the strike, dip, and rake calculated by the FPFIT program (Reasenberg and Oppenheimer, 1985) are 7°, 5°, and 10°, respectively. The focal mechanisms plotted in a Frohlich triangle diagram show that most of them are extensional-force dominated, and only few of them are strike-slip and thrust-force dominated (Fig. 4c). The strikes of the focal mechanisms are mostly in north-northeast direction, parallel to that of the aftershock sequence (Fig. 4a,b). The steep dips toward the west of one of the nodal planes of the focal mechanisms also coincide with that of the aftershock sequence (Fig. 4b,f–h). To describe the focal mechanisms of the aftershock sequence in detail, we further divided the 523 focal mechanisms into five groups, based on their event clusters and the types of focal mechanisms, from north to south (Fig. 4e). We used the FaultKin7 software (see Data and Resources) to calculate the composite focal mechanisms (CFMs) of these five groups from their P and T axes (Fig. 4d). The Hualien group is located in the west of the Milun fault, and the CFM was calculated from the P and T axes of 145 focal mechanisms. Based on the distribution of the aftershocks (Fig. 4f), we chose a steep dipping to the west of the nodal plane as the fault plane. The average orientation of the fault plane of this group from the CFM is a 27.5° (north-northeast) strike with a 73.5° dip toward the west. Two strike-slip-dominated groups were determined between the Hualien and Jian groups: one group (Nanbin1) with 23 focal mechanisms located at a depth shallower than 4 km at the southern tip of Milun fault and the other one (Nanbin2) with 9 focal mechanisms located at depths ranging from 4 to 10 km. The Nanbin1 group is the only group recorded at shallower depths (0–4 km). The strike of the nodal plane related to the aftershocks is north-northeast (31.3°), with a steep dip (79.4°) to the west. The Nanbin2 group has a right-lateral nodal plane, with a 97.7° strike (east–west) and nearly vertical dip (83.3°); it was chosen as a fault plane, based on the distribution of the events. The Jian group is located on the east side of the CeR and includes 153 focal mechanisms. One of the nodal planes that was selected as the fault plane has a 33.1° (north-northeast) strike with a 73.5° dip toward the west, based on the aftershock distribution (Fig. 4g). The last group, the Shoufeng group, includes 193 events and is mostly situated west of the Lingding fault. It can be chosen as the fault plane because of the 47.2° (north-northeast) strike of this group, with a steep west dip (80.9°; Fig. 4h). The extension-dominated focal mechanisms of the Hualien, Jian, and Shoufeng groups show the main feature of the aftershock sequence. The average strikes of the nodal planes of these three groups are north-northeast, which is consistent with the distribution of the aftershock sequence. It is interesting to note that the average north-northeast strikes of these three groups have a clockwise rotation (27.5°–47.2°) from north to south and a steep dip to the west (Fig. 4e).

DISCUSSION

The behavior of the aftershock sequence of the Hualien earthquake is more complex than that of other simple fault ruptures of large earthquakes, for example, the 2003 M_w 6.4 Chengkung earthquake that occurred in the south of eastern Taiwan: the focal mechanisms of the mainshock, distribution of aftershocks, and surface deformation can be easily explained and modeled by a simple east-dipping fault model (Kuochen *et al.*, 2004; Wu *et al.*, 2006; Hu *et al.*, 2007). However, the strike slip with a thrust type of focal mechanism of the mainshock of the Hualien earthquake is different from the extensional type of focal mechanisms of the aftershocks. However, all focal mechanisms have a similar north-northeast strike with a steep west dip and even similar event depths (5–15 km; Fig. 5a). This implies that the mainshock and aftershocks could move along with the same west-dipping interface but with different senses of fault movements (Fig. 5).

Recently, Chen *et al.* (2014) used Global Positioning System (GPS) measurements from 25 stations in Hualien from 2007 to 2009 to show that the north-northwest-trending shortening principal axis is due to the collision between the EUP and PSP, which is similar to the results of a study based on focal mechanisms (Wu *et al.*, 2009). Also, the shear-strain analysis shows that the north-northeast-trending sinistral shearing that dominates this region coincides with the strikes of the Milun and Lingding faults. However, it is interesting to note that the north-northeast strike of the mainshock, with a left-lateral strike-slip component, is consistent with those of the interseismic strain field calculated from GPS measurements for the 1951 M_L 7.3 Hualien earthquake and the Milun and Lingding faults, except for the west-dipping rupture of the 2018 M_w 6.4 mainshock. This could imply that the shallow fault structures (Milun and Lingding faults) could be part of the flower structures of a big strike-slip fault system. The main structure might be related to the mainshock at a depth of 10 km and might have triggered the surface deformation along the Milun and Lingding faults. However, because the surface deformation data set has not been published, we cannot further discuss the relationship between surface deformation and aftershocks.

Based on the comparison of the background seismicity with the aftershock sequence, Kuochen *et al.* (2004) and Shyu *et al.* (2016) showed that the seismicity patterns in the Hualien area are scattered (Fig. 4f–h), although some event clusters with mostly thrust-type focal mechanisms can be identified from their studies. The behavior of the aftershock sequence completely differs from that of the background seismicity, in terms of the event patterns and focal mechanisms (Fig. 4f–h). This aftershock sequence is a new event cluster triggered by the mainshock of the Hualien earthquake but may have pre-existed because the relatively complete earthquake catalog in Taiwan has been established since 1991. The location errors are within 0.6 km at both horizontal and depth directions from Kuochen *et al.* (2004) and Shyu *et al.* (2016). Therefore, the location problem can be ruled

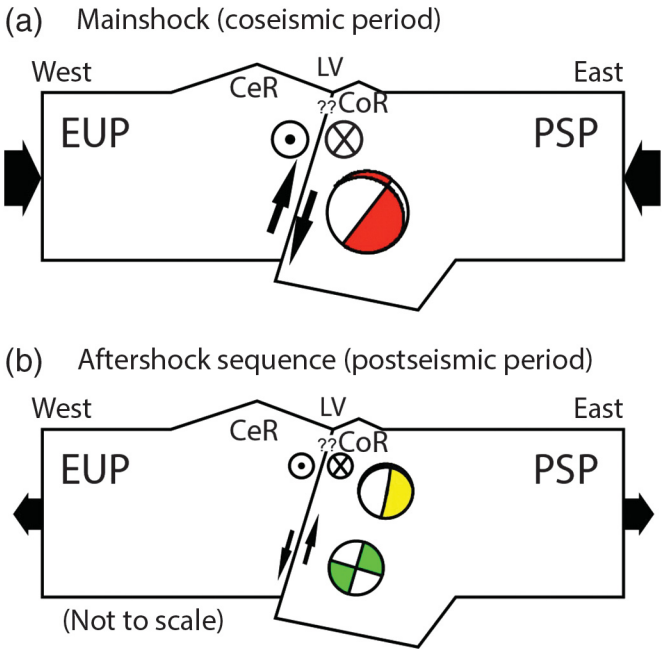

▲ **Figure 5.** The fault type and stress changes between the (a) mainshock and (b) aftershock sequence. (a) During the coseismic period, the Hualien area was under compressional stress, and the rupture was a left-lateral strike slip with thrust component, with a high-angle west-dipping plane. (b) During the postseismic period, the Hualien area was under extensional stress, and the rupture was the same as that of the mainshock but mostly dominated by normal faulting. Yellow focal mechanism, Nanbin1 group in Figure 4g; green focal mechanism, Hualien group in Figure 4f.

out when we compare the earthquake locations between the background seismicity and the aftershock sequence. The rupture propagated southward to the Hualien area and may mark the locations of the plate boundary. Based on the left-lateral thrust focal mechanism of the mainshock as a coseismic period, the northwestward-subducting PSP beneath the EUP was initially oriented along the steeply west-dipping plane (Fig. 5a). Subsequently, postseismic stress relaxation occurred along the same plane in a short period of time, based on the extensional focal mechanisms of the aftershocks (Fig. 5b). These stress changes in subduction zones have been observed in some places: for examples, the thrust faults of the 1978 M_w 7.8 Oaxaca and the 1985 M_w 8.1 Michoacán earthquakes, followed by the 1999 M_w 7.5 and the 1997 M_w 7.1 normal-faulting earthquakes, respectively (Mikumo *et al.*, 2002). But these two examples show a long postseismic stress-relaxation time compared with that of the 2018 Hualien earthquake. However, the phenomenon of the 2018 Hualien earthquake is similar that of the 1986 Hualien earthquake (Yu and Cheng, 1997). Yu and Cheng (1997) showed a short relaxation time of asthenosphere from numerical modeling based on the migration pattern and short time duration (tens of day) of aftershocks of 1986 Hualien earthquake reported by (Liaw *et al.*, 1986). They argued that this rapid stress change might be related to the crustal material rich in quartz or water. Also, as predicted by Yu and Cheng (1997), the recurrence time of large earthquakes is ~20–30 yrs, due to the short relaxation time. Based on historical records, the large earthquakes that occurred in 1951, 1986, and 2018 indicate a recurrence time of 30 yrs in this area. However, this is one of possible hypotheses from a study of the 1986 Hualien earthquake, and the further surface deformation observations from GPS and Interferometric Synthetic Aperture Radar for the postseismic period are needed for testing this model.

CONCLUSIONS

In this study, we located 2192 aftershocks and made 580 focal mechanisms for a period of 2–14 days after the mainshock, using a temporary dense seismic network in the southern part of the aftershock area. Although some unpicked events were buried in coda waves, which require more sophisticated methods to be processed later, this data set has already provided unique and fundamental information for the investigation of seismogenic structures in the Hualien area. Because the focal mechanisms provide important information about the stress pattern in this area, the polarities of the first *P*-wave motions were checked carefully. The characteristics of the aftershock sequence can be summarized as follows:

1. Most of the aftershocks occurred on land along the LV and extended southward to ~23.8°N (Shoufang township). The depths of the aftershocks mostly range from 5 to 15 km, and only few are above 5 km.
2. Most of the focal mechanisms determined by the first *P*-wave polarities are normal faulting that differs from that of the mainshock (strike slip with thrust faulting).
3. Based on the distribution of the aftershocks and focal mechanisms between 5 and 15 km depth, a north-northeast strike with steep west-dipping of the nodal planes might be the orientation of the normal-fault plane. Above a depth of 5 km, a north-northeast strike with steep west dipping of the nodal planes might be the orientation of the left-lateral strike-slip fault plane.
4. Based on the focal mechanisms, the north-northwest-shorting principal axis (P axis) during the interseismic period changed to a north-northwest-extensional principal axis (T axis) during the postseismic period.

DATA AND RESOURCES

All data used in the article were listed in the Ⓔ electronic supplement to this article. Seismograms used in this study can be obtained from the corresponding author Hao Kuo-Chen (kuochen@ncu.edu.tw). The other data are obtained from the following websites: the U.S. Geological Survey moment tensor catalog (https://earthquake.usgs.gov/), the Central Weather Bureau (https://scweb.cwb.gov.tw), the FaultKin7 software (http://www.geo.cornell.edu/geology/faculty/RWA/programs/faultkin.html), and the real-time moment tensor inversion system (http://rmt.earth.sinica.edu.tw).

ACKNOWLEDGMENTS

The authors thank Wen-Yen Chang of National Dong Hua University, Yu-ting Kuo and Mr. Chin-Shang Ku of the IES, Academia Sinica, and Hsuan-Yu Kuo of the National Central University for the assistance of the field deployment. H. K.-C. is supported by MOST (MOST 104-2628-M-008-005-MY3 and MOST 107-2628-M-008 -004 -MY3).

REFERENCES

Brown, R. J., R. R. Stewart, J. E. Gaiser, and D. C. Lawton (2000). An acquisition polarity standard for multicomponent seismic data, *CREWES Research Report*.

Chen, C. Y., J. C. Lee, Y. G. Chen, and R. F. Chen (2014). Campaigned GPS on present-day crustal deformation in northernmost Longitudinal Valley preliminary results, Hualien Taiwan, *Terr. Atmos. Ocean. Sci.* **25,** 337–357, doi: 10.3319/TAO.2013.12.25.01(TT).

Chen, K. J. (1998). *S*-wave attenuation structure in the Taiwan area and its correlation to seismicity, *Terr. Atmos. Ocean. Sci.* **9,** no. 1, 97–118.

Chen, K. J., Y. H. Yeh, and C. T. Shyu (1996). Q_P structure in the Taiwan area and its correlation to seismicity, *Terr. Atmos. Ocean. Sci.* **7,** no. 4, 409–429.

Chen, Y. L., and T. C. Shin (1998). Study on the earthquake location of 3-D velocity structure in the Taiwan area, *Meteorol. Bull.* **42,** no. 2, 135–169.

Chin, S. J., J. Y. Lin, Y. F. Chen, W. N. Wu, and C. W. Liang (2016). Transition of the Taiwan-Ryukyu collision-subduction process as revealed by ocean-bottom seismometer observations, *J. Asian Earth Sci.* **128,** 149–157.

Frohlich, C. (1992). Triangle diagrams: Ternary graphs to display similarity and diversity of earthquake focal mechanisms, *Phys. Earth Planet In.* **75,** 193–198.

Havskov, J., and L. Ottemoller (1999). SeisAn earthquake analysis software, *Seismol. Res. Lett.* **70,** no. 5, 532–534.

Havskov, J., and L. Ottemoller (2010). *Routine Data Processing in Earthquake Seismology*, Springer, Dordrecht, The Netherlands.

Hsu, T. L. (1955). Earthquakes in Taiwan, *Q. J. Bank Taiwan* **7,** no. 2, 148–164 (in Chinese).

Hsu, T. L. (1962). Recent faulting in the Longitudinal Valley of eastern Taiwan, *Geol. Soc. China Mem.* **1,** 95–102.

Hu, J.-C., L.-W. Cheng, H.-Y. Chen, Y.-M. Wu, J.-C. Lee, Y.-G. Chen, K.-C. Lin, R.-J. Rau, H. Kuochen, H.-H. Chen, *et al.* (2007). Coseismic deformation revealed by inversion of strong motion and GPS data: The 2003 Chengkung earthquake in eastern Taiwan, *Geophys. J. Int.* **169,** 667–674.

Kuochen, H., Y. M. Wu, C. H. Chang, J. C. Hu, and W. S. Chen (2004). Relocation of the eastern Taiwan earthquakes and its tectonic implications, *Terr. Atmos. Ocean. Sci.* **15,** 647–666, doi: 10.3319/TAO.2004.15.4.647(T).

Lee, S. J., Q. Liu, J. Tromp, D. Komatitsch, W. T. Liang, and B. S. Huang (2014). Toward real time regional earthquake simulation II: Real-time online earthquake simulation (ROS) of Taiwan earthquakes, *J. Asian Earth Sci.* **87,** 56–68.

Liaw, Z. S., C. S. Wang, and Y. T. Yeh (1986). A study of aftershocks of the 20 May 1986 Hualien earthquake, *Bull. Inst. Earth Sci.* **16,** 15–28.

Lienert, B. R. E., E. Berg, and L. N. Frazer (1986). Hypocenter: An earthquake location method using centered, scaled and adaptively least squares, *Bull. Seismol. Soc. Am.* **76,** 771–783.

Lin, C. W., W. S. Chen, Y. C. Liu, and P. T. Chen (2009). Active faults of eastern and southern Taiwan, *Spec. Publ. Central Geol. Surv.* **23,** MOEA, Taiwan.

Mikumo, T., Y. Yagi, S. K. Singh, and M. A. Santoyo (2002). Coseismic and postseismic stress changes in a subducting plate: Possible stress interactions between large interplate thrust and intraplate normal-faulting earthquakes, *J. Geophys. Res.* **107,** no. B1, doi: 10.1029/2001JB000446.

Reasenberg, P. A., and D. H. Oppenheimer (1985). FPFIT, FPPLOT, and FPPAGE: Fortran computer programs for calculating and displaying earthquake fault-plane solutions, *U.S. Geol. Surv. Open-File Rept. 85-739*.

Shyu, J. B. H., C. F. Chen, and Y. M. Wu (2016). Seismotectonic characteristics of the northernmost Longitudinal Valley, eastern Taiwan: Structural development of a vanishing suture, *Tectonophysics* **692,** 295–308.

Theunissen, T., Y. Font, S. Lallemand, and W. T. Liang (2010). The largest instrumentally recorded earthquake in Taiwan: Revised location and magnitude, and tectonic significance of the 1920 event, *Geophys. J. Int.* **183,** no. 3, 1119–1133.

Tsai, Y. B. (1986). Seismotectonics of Taiwan, *Tectonophysics* **125,** 17–28.

Wu, F. T., W.-T. Liang, J.-C. Lee, H. Benz, and A. Villasenor (2009). A model for the termination of the Ryukyu subduction zone against Taiwan: A junction of collision, subduction/separation, and subduction boundaries, *J. Geophys. Res.* **114,** no. B07404, doi: 10.1029/2008JB005950.

Wu, Y. M., C. H. Chang, L. Zhao, J. B. H. Shyu, Y. G. Chen, K. Sieh, and J. P. Avouac (2007). Seismic tomography of Taiwan: Improved constraints from a dense network of strong-motion stations, *J. Geophys. Res.* **112,** no. B08312, doi: 10.1029/2007JB004983.

Wu, Y. M., Y. G. Chen, T. C. Shin, H. Kuochen, C. S. Hou, C. H. Chang, C. F. Wu, and T. L. Teng (2006). Coseismic vs. interseismic ground deformations, faults rupture inversion and segmentation revealed by 2003 M_w 6.8 Chengkung earthquake in eastern Taiwan, *Geophys. Res. Lett.* **33,** L02312, doi: 10.1029/2005GL024711.

Yu, S. B., D. D. Jackson, G. K. Yu, and C. C. Liu (1990). Dislocation model for crustal deformation in the Longitudinal Valley area, eastern Taiwan, *Tectonophysics* **183,** 97–109, doi: 10.1016/0040-1951(90)90190-J.

Yu, T. T., and S. N. Cheng (1997). Stress diffusion and spatial migration of aftershocks in the Hualien area, Taiwan, *Terr. Atmos. Ocean. Sci.* **8,** 31–48.

Hao Kuo-Chen
Zhuo-Kang Guan
Pei-Yu Jhong
Department of Earth Sciences
National Central University
Taoyuan City, Taiwan
kuochen@ncu.edu.tw
s12085240@hotmail.com
py10662020@g.ncu.edu.tw

Wei-Fang Sun
Department of Natural Resources and Environmental Studies
National Dong Hwa University
Hualien City, Taiwan
ttsun.sun@gmail.com

Dennis Brown
Institute of Earth Sciences
Jaume Almera, ICTJA-CSIC
08028 Barcelona, Spain
dbrown@ictja.csic.es